



On the Mechanism of Drag Reduction in Fully-Developed Turbulent Channel Flow with a Streamwise Micro-featured Superhydrophobic Wall

M. Saadat-Bakhsh[†], N. M. Nouri and H. Norouzi

Mechanical Engineering, Iran University of Science and Technology, Tehran, Iran

[†]Corresponding Author Email: a.saadatbakhsh@gmail.com

(Received February 26, 2017; accepted April 16, 2017)

ABSTRACT

The superhydrophobic drag reduction changes the structures of turbulent flow. However, the underlying mechanism is not clear. The aim of this study is to determine the alternations of turbulent flow due to applying a streamwise micro-featured superhydrophobic wall. Large eddy simulations are performed to explore the effect of micro-features on near-wall behaviors. The results indicate that the outward motion of the lifted low-speed streaks is restricted to the lower wall layers, and the region of maximum production of streamwise vorticities is shifted toward the micro-featured wall. The quadrant analysis of Reynolds stress shows that there is a stronger increase in outward motion of high-speed fluid and inward motion of low-speed fluid than ejection and sweep.

Keywords: Superhydrophobic surface; Drag reduction mechanism; Coherent structures; Streak strength.

NOMENCLATURE

d	micro-feature's width	y	wall-normal direction
DR	drag reduction	y^+	dimensionless wall distance of the grid points
H	channel height	z	spanwise direction
L	channel length		
Q	the second invariant of velocity gradient tensor ∇u	Δx	grid spacing in the x direction
$R_{uu}(\Delta z)$	spanwise correlation coefficient of streamwise velocity fluctuation	Δy	grid spacing in the y direction
$R_{vv}(\Delta z)$	spanwise correlation coefficient of wall-normal velocity fluctuation	Δz	Grid spacing in the z direction
$R_{ww}(\Delta z)$	spanwise correlation coefficient of spanwise velocity fluctuation	ν	kinematic viscosity
$Re_\tau = u_\tau \delta / \nu$	friction Reynolds number	δ	channel half height
RMS	root Mean Square	τ_w	averaged wall shear stress of no-slip wall and superhydrophobic wall of the channel
U_{slip}	slip velocity	τ_{wB}	wall shear stress of the bottom wall (superhydrophobic wall)
$U_{Mean}^+ = U / u_\tau$	dimensionless form of the mean velocity by friction velocity	λ_2	the second eigenvalue of the symmetric tensor $S^2 + \Omega^2$; where S and Ω are respectively the symmetric and antisymmetric velocity gradient tensor ∇u
u_τ	friction velocity	θ	inclination angle of the vortex lines on the streak flank (as a measure of streak strength)
u	streamwise velocity fluctuation		
\overline{uv}	time averaged of Reynolds stress		
v	wall-normal velocity fluctuation		
W	channel width		
w	spanwise velocity fluctuation		
w	shear-free width of the wall	ω_{x-RMS}	RMS of streamwise vorticity
x	streamwise direction		

ω_{Y-RMS}	RMS of wall-normal vorticity	$\bar{\quad}$	time averaged
ω_{Z-RMS}	RMS of spanwise vorticity	...	

1. INTRODUCTION

The issue of whether superhydrophobic drag reduction changes the turbulent flow statistics has been addressed by several authors. Several works have used Navier's slip boundary condition to investigate the effects of the slip condition at the superhydrophobic wall using direct numerical simulation (DNS) and large eddy simulation (LES) (Min *et al.* 2004, Nouri *et al.* 2013). In these simulations, the slip length is used to model the macroscopic effects of the superhydrophobic surface on the flow. Since surface roughness and chemical hydrophobicity themselves can result in drag reduction, some other researchers have tried to simulate the individual effect of surface roughness on flow quantities. In these works, a shear-free air-water boundary condition is used instead of Navier's slip condition (Jeffs *et al.* 2010, Martell *et al.* 2009, 2010, Park *et al.* 2013), and Türk *et al.* 2014). On the other hand, the drag and heat transfer-enhancing effect of near-wall coherent structures is widely acknowledged. These coherent structures sweep near-wall fluid toward the wall and eject it away from the wall. Consequently, it is necessary to understand the near-wall behaviors of coherent structures due to superhydrophobicity.

A study conducted on Navier's slip boundary condition of turbulent channel flow reported that the streamwise slip condition resulted in the reduction of drag, while the spanwise slip condition increased the drag. To achieve a noticeable reduction of drag, the slip length must be greater than a certain value (Min and Kim, 2004). A theoretical formulation was presented to predict the relationship between change in reduction in drag and streamwise and spanwise slip length in fully-developed turbulent channel flow (Fukagata *et al.* 2006). The DNS of a turbulent channel flow at different streamwise and spanwise slip lengths and $Re_\tau = 180, 360$ were conducted in (Busse and Sandham, 2012). This study showed that the drag-reducing and drag-increasing effects of superhydrophobic surfaces depended on the relative magnitude of the streamwise and spanwise slip lengths (Busse and Sandham (2012)). Another work using Navier's slip condition suggested that the effectiveness of superhydrophobic drag reduction was increased with an increasing Reynolds number (nearly 1, 9, and 27% for the friction Reynolds numbers of 180, 395, and 500, respectively, at the slip length of $10 \mu m$) (Nouri *et al.* 2013). The performance and mechanism of superhydrophobic drag reduction of micro-featured superhydrophobic wall were investigated at different Reynolds numbers using DNS in (Martell *et al.* 2010).

Neither the Reynolds number nor the physical gap dimension of micro-features could determine the shear stress reduction, while the gap sizing in the wall units was the main parameter that can be assigned the drag reduction value (Martell *et al.* 2010). Drag reduction in the turbulent channel flow was associated with the effective slip length normalized by viscous wall units. This investigation was performed using streamwise micro-ridges placed at the bottom wall of the channel (Park *et al.* 2013). Also, the streamwise vorticity production and the generation mechanism of secondary flow due to micro-structure superhydrophobicity were investigated through DNS (Türk *et al.* 2014).

As mentioned above, it is accepted that applying superhydrophobic surfaces leads to drag reduction; however, the underlying mechanisms must be studied more particularly. In our research, we investigated the principal mechanisms of the superhydrophobic drag reduction of micro-featured surfaces using large eddy simulation of fully-developed turbulent channel flow. Sections 2 and 3 present the computational details and validation process. Section 4 is dedicated to the discussion of the results. In this section, first, the influence of a micro-featured surface on the mean velocity profile, drag reduction, and slip velocity is addresses, and Reynolds stresses are considered. Finally, to explore the alternation of near-wall behaviors, the correlation coefficient and near-wall vortical structures are considered. Our concluding remarks are presented in Section 5.

2. COMPUTATIONAL APPROACH

Fully-developed turbulent channel flow is designed to explore the role of micro-features in the near-wall turbulent characteristics. 0 shows the physical geometry of the channel with micro-features placed at the bottom wall. The friction Reynolds number of the turbulent channel flow based on the channel half-length was 180. The periodic boundary condition was applied in the streamwise (x) and spanwise (z) directions. A no-slip wall was applied at the top of the channel. At the bottom wall, a shear-free condition was used at the water-air interface, and a regular no-slip condition was applied to the remaining bottom wall. In all simulations, the dimensions of the computational domain were selected in such a way that they were nearly $6\delta \times 2\delta \times 3\delta$ (δ is the channel half height) in the x , y , and z directions, respectively. Table 1 indicates that the spanwise length of the slip channel $w/d = 2$ (case 5) was a bit greater than that of the other cases. Uniform grid points were used in the x and z directions.

Table 1 Grid resolution of simulation cases; case 1: no-slip; cases 2-6: slip

Case number	d (μm)	w (μm)	Grid size	Δx^+	Δy^+_{min}	Δz^+
1 (no-slip)	-	-	64×64×128	16.9	0.4	4.2
2 (slip)	30	30	64×64×128	16.9	0.4	4.2
3 (slip)	30	30	64×128×256	16.9	0.1	2.1
4 (slip)	30	30	128×128×256	8.4	0.1	2.1
5 (slip)	30	60	64×128×264	16.9	0.1	2.1
6 (slip)	30	90	64×128×256	16.9	0.1	2.1

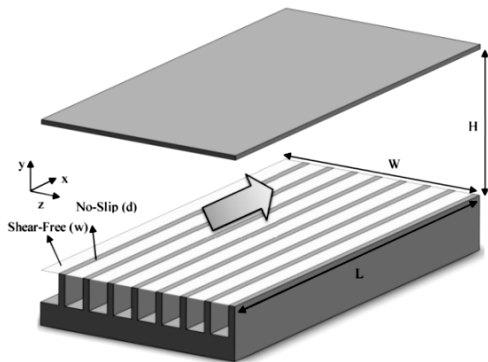


Fig. 1. Schematic representations of channel flow with micro-ridges placed in the bottom wall.

The filtered equations were solved using open-source computational fluid dynamics (CFD) code called OpenFOAM. This computer code uses the finite volume method and has been validated extensively for the LES method. Since in the turbulent channel flow there is no notable sensitivity to the sub-grid scale models the dynamic Smagorinsky sub-grid model (Germano *et al.* 1991) is used based on the rigorous considerations. To eliminate the pressure-velocity coupling, the pressure implicit with the splitting of operator (PISO) algorithm was applied. The second-order method was used for the convection and diffusion, and the second-order backward method was used for time integration. Since the flow was periodic in the x and z, all of the filtered variables were time-averaged and, then, ensemble averaged in the streamwise and spanwise directions. Hence, the velocity profile, slip velocity, and the Reynolds stresses were calculated as follows:

$$U_{Mean}(y) = \frac{1}{L_x L_z} \int_0^{L_z} \int_0^{L_x} \bar{U}(x, y, z) dx dz \quad (1)$$

$$U_{bulk} = \frac{1}{L_y} \int_0^{L_y} U_{Mean}(y) dy \quad (2)$$

$$R_{ij} = \frac{1}{L_x L_z} \int_0^{L_z} \int_0^{L_x} \bar{R}_{ij}(x, y, z) dx dz \quad (3)$$

$$U_{slip} = \frac{1}{L_x L_z} \int_0^{L_z} \int_0^{L_x} \bar{U}(x, y = 0, z) dx dz \quad (4)$$

Where \bar{U} and \bar{R}_{ij} are the time-averaged streamwise velocity component and the Reynolds stresses tensor, respectively; L_x , L_y , and L_z are the streamwise, wall-normal, and spanwise lengths of the channel, respectively. The grid resolution and grid spacing of the simulation cases are given in Table 1. Based on the time-averaged spatial correlations the time scale of 40 flow through the channel (40*channel length/bulk flow velocity) is enough to averaging the flow variables.

3. GRID STUDY AND CODE VALIDATION

All of the grid configurations are listed in Table 1. To validate the current code, before applying micro-features at the bottom wall, the no-slip results (case 1) were compared with the DNS of fully-developed turbulent channel flow at the friction Reynolds number of 180 (Kim *et al.* 1987). Fig. 1(a) illustrates good agreement in the mean velocity between the no-slip DNS results and the LES simulation. In Fig. 1(b)-(d), the RMS of the velocity fluctuations was compared with those of the DNS data. The simulation parameters of the fully-developed turbulent channel flow over a micro-featured superhydrophobic wall were similar to those of the regular channel, but the shear-free condition was applied at the air-water interface instead of the no-slip condition used on the whole bottom wall.

4. RESULTS AND DISCUSSION

To detect changes in the turbulent structures, we compared the no-slip and micro-featured superhydrophobic results. The comparisons were made for mean flow quantities, such as mean velocity profiles, drag reduction, slip velocity, and turbulence statistics. In addition, spatial correlation coefficients, integral length scales, streamwise vortical structures, and streak instability were analyzed to explore the changes in the turbulent structures.

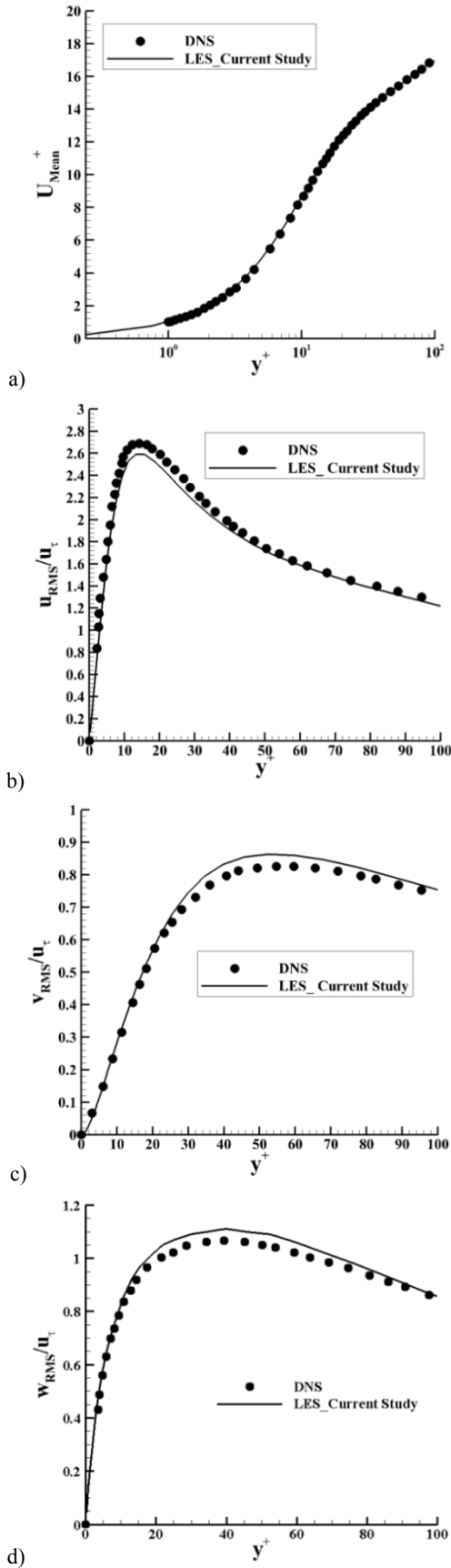


Fig. 1. DNS (Kim *et al.* (1987)) and present results of no-slip channel: (a) Mean velocity; (b) u_{RMS} ; (c) v_{RMS} ; (d) w_{RMS} .

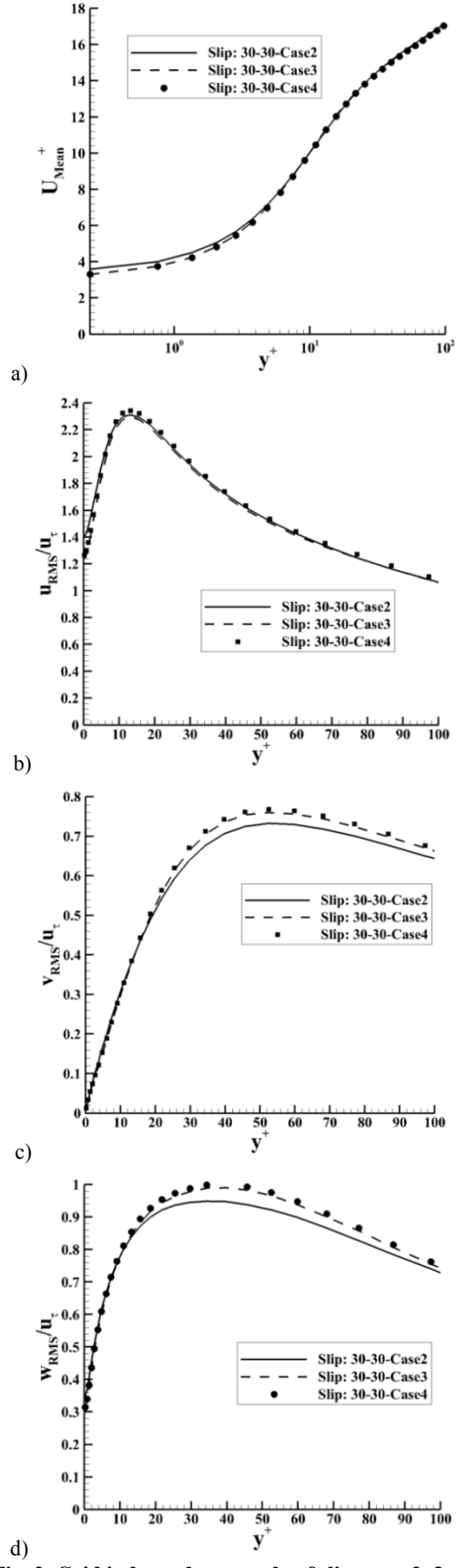


Fig. 2. Grid independence study of slip cases 2, 3, and 4: (a) Mean velocity; (b) u_{RMS} ; (c) v_{RMS} ; (d) w_{RMS} .

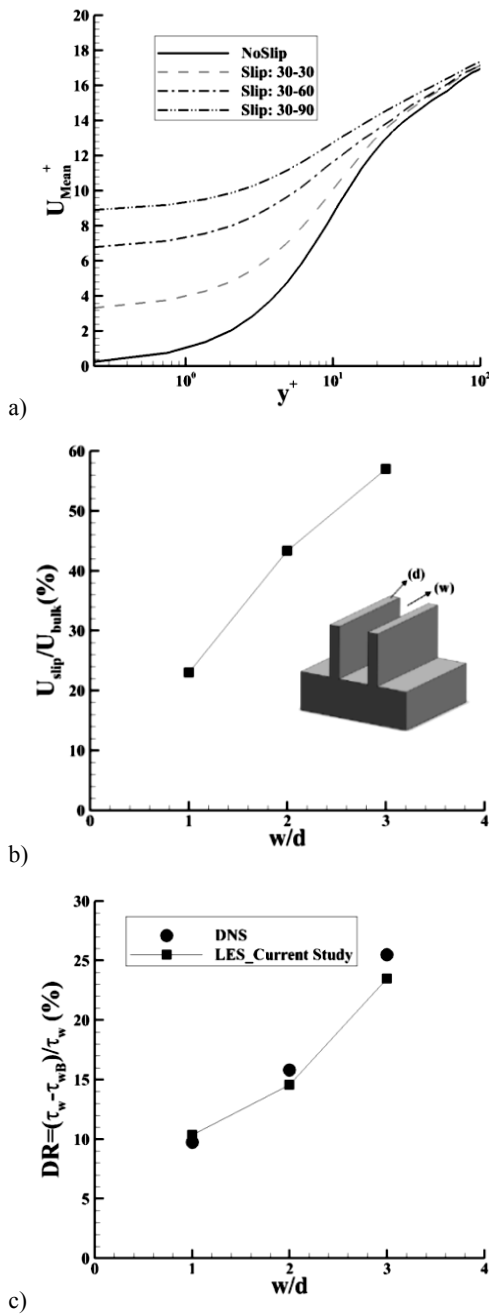


Fig. 3. (a) Mean velocity over no-slip and superhydrophobic channels (b) Slip velocity in the superhydrophobic wall; (c) frictional drag reduction of DNS (Martell *et al.* (2009)), and the current simulation.

4.1. Mean Flow

Fig. 3(a) illustrates the mean flow velocity profile in the wall units. Based on the figure, the slip velocity was increased as the ratio of shear-free to no-slip (w/d) increased. The overall shape of the velocity profile did not change, but the velocity gradient between the viscous sublayer and the buffer layer was decreased. Fig. 3(b) illustrates that the slip velocity was increased with w/d from 23 to 57% of the bulk velocity for $w/d = 1$ to 3. Fig. 3(c) shows the drag reduction of the turbulent channel.

Note that, when the mass flow rate is kept constant through simulations, the velocity at the top wall decreased as the slip velocity of the bottom wall increased. So, the average shear stress of the bottom wall and the top wall of the channel, $\tau_w = (\tau_{wB} + \tau_{wT})/2$, and the shear stress on the bottom wall, τ_{wB} , could be used to calculate the drag reduction values. Drag reductions were nearly 10, 18, and 26% for $w/d = 1, 2,$ and $3,$ respectively. The drag reduction values were compared with the DNS simulation of (Martell *et al.* (2009)). Also, the non-linear reduction in shear stress might be related to the nonlinearity effects of near-wall turbulence phenomena.

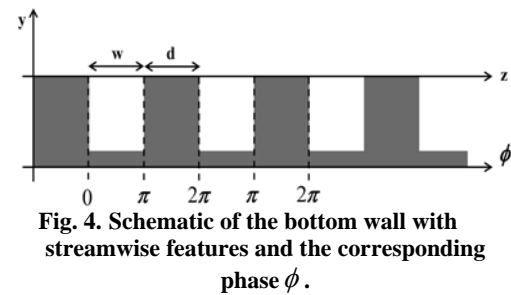


Fig. 4. Schematic of the bottom wall with streamwise features and the corresponding phase ϕ .

4.2. Turbulence Statistics Of Superhydrophobic Channel

4.2.1. Triple Decomposition of Velocity Field

Since the bottom wall boundary condition was periodic in the spanwise direction for the superhydrophobic channels, it was expected that the statistical structures of the turbulent velocity field to show similar periodicity. So, to explore the alternations of the turbulent flow structures, this periodic behavior had to be removed. Accordingly, triple decomposition, proposed by Reynolds and Hussain (Reynolds and Hussain (1972)), which represents a flow field as a sum of three components according to:

$$f = \bar{f} + \tilde{f} + f' \quad (5)$$

was used, where f is an arbitrary variable and a function of space and time, \bar{f} is the time-averaged component, \tilde{f} is the periodic or coherent fluctuations, and f' is the turbulent or random fluctuations. Here, \tilde{f} is defined by phase averaging the data in the spanwise direction resulting in $\langle f \rangle$ such that $\tilde{f} = \langle f \rangle - \bar{f}$. Hence, $\langle f \rangle$ is defined as follows:

$$\langle f \rangle(y, \phi) = \frac{1}{N} \sum_{n=1}^N \int \int_x f(x, y, L(\frac{\phi}{2\pi} + n), t) dx dt \quad (6)$$

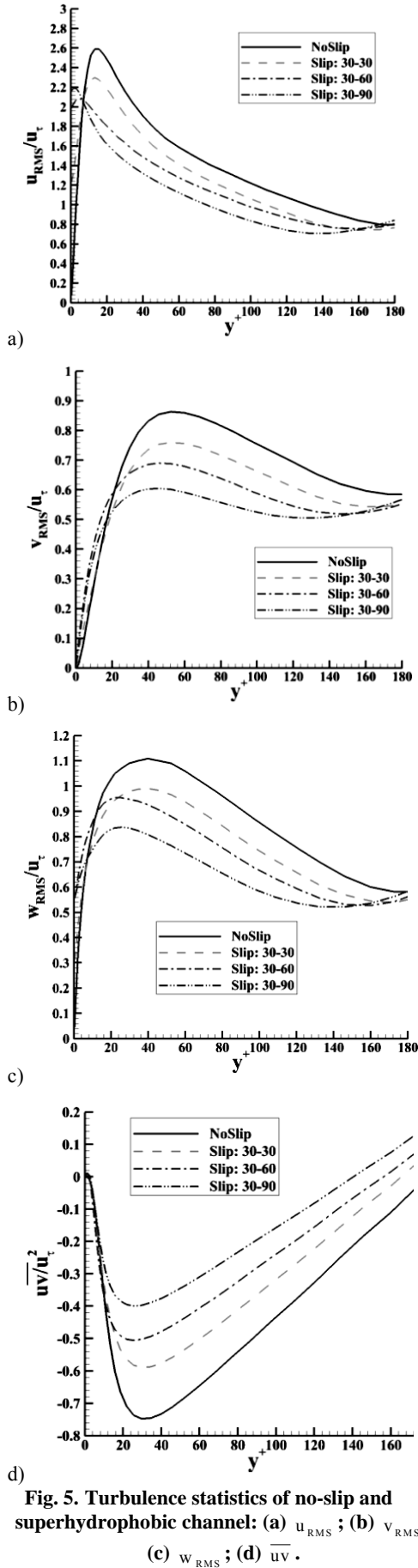


Fig. 5. Turbulence statistics of no-slip and superhydrophobic channel: (a) u_{RMS} ; (b) v_{RMS} ; (c) w_{RMS} ; (d) \overline{uv} .

where ϕ is a phase with respect to the periodic structure as shown in Fig. 4, and N is the number of periods in the computational domain. Averaging $\langle f \rangle$ over ϕ results in the spatial mean:

$$\bar{f}(y) = \frac{1}{2\pi} \int_0^{2\pi} \langle f \rangle(y, \phi) d\phi \quad (7)$$

Accordingly, coherent fluctuations are defined as:

$$\tilde{f}(y, \phi) = \langle f \rangle(y, \phi) - \bar{f}(y) \quad (8)$$

Thus, any flow quantity can be decomposed as follows:

$$f(x, y, z, t) = \langle f \rangle(y, \phi) + f''(x, y, z, t) = \bar{f}(y) + \tilde{f}(y, \phi) + f''(x, y, z, t) \quad (9)$$

where f'' represents the deviation from the phase average, which is referred to as random fluctuation. Hence, the overall fluctuation is defined as the deviation from the spatial mean:

$$f'(x, y, z, t) = f(x, y, z, t) - \bar{f}(y) = \tilde{f}(y, \phi) + f''(x, y, z, t) \quad (10)$$

To explore the turbulent flow statistics and structures, the periodic behavior of the bottom wall boundary condition was removed from the velocity field, and all of the results were presented without this periodic behavior. As demonstrated in the Fig. 5, the peak of the RMS of the fluctuating components was decreased and moved toward the wall. Note that these changes were greater for the streamwise component. Fig. 5(d) indicates the Reynolds stress \overline{uv} normalized by u_τ^2 . It is apparent from this figure that the peak of the profile was reduced and became closer to the superhydrophobic wall. Note that this shift affected the streak instability cycle and subsequent production of the streamwise vortical structures. The results of drag reduction and Reynolds stresses were consistent with those of previous studies (Martell *et al.* (2009)). In their simulations, the pressure gradient of the turbulent channel was constant through simulations, while the flow rate was constant in our study. So, a precise comparison could not be made between the turbulent statistics; however, Fig. 3(b) compares the drag reduction of our study and (Martell *et al.* (2009)).

4.3. Turbulence Structures

Based on the results of the fluctuating velocity component and Reynolds stresses, it was hypothesized that the buffer layer is shifted to lower values in the wall units; so, the turbulence was extended to wider areas of the channel. To test this hypothesis, the streamwise coherent structures were investigated. Fig. 6 illustrates the near-wall streamwise vortices, indicated by the λ_2 vortex definition criteria in the region $0 < y^+ < 60$. Also, for illustrative purposes, it was useful to represent

the 'strength' of lifted streaks (i.e., the magnitude of streak wall-normal vorticity $\omega_y = \partial U / \partial z$) in terms of vortex line inclination angle θ (hereafter called streak strength) on the streak flank, given locally by $\theta = \tan^{-1}(|\omega_y|/|\omega_z|)$. The λ_2 isosurfaces were colored by θ magnitude in Fig. 6(a)-(b). As indicated by this figure, the near-wall density of the streamwise vortices was decreased by introducing superhydrophobicity and the place of maximum presence of the quasi-streamwise vortices was shifted to smaller y^+ . To see these alterations, the structures that were aligned near the bottom wall and top wall could be compared. Fig. 8(a) demonstrates the existence of coherent structures using the second invariant of velocity gradient tensor Q . The peak of Q was appropriate to the dominant presence of coherent structures. As indicated in Fig. 8(a), the peak of Q was shifted to the superhydrophobic wall due to surface features; it can be concluded that coherent structures were moved toward the bottom wall, which confirms our hypothesis that the buffer layer was shifted to lower values in the wall units due to superhydrophobicity, and turbulence was extended to wider areas of the channel.

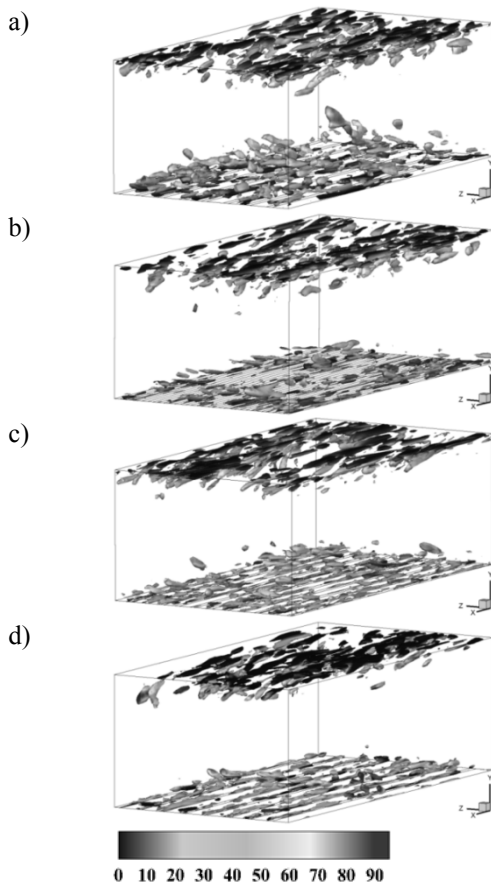


Fig. 6. Streamwise vortices indicated by the isosurfaces of $\lambda_2 = 4 \times 10^9$ vortex definition (Jeong and Hussain (1995)) colored by the inclination angle of the vortex lines: (a) No-slip; (b) Slip: 30-30; (c) Slip: 30-60; (d) Slip: 30-90.

The streak strength of low-speed streaks was increased by introducing superhydrophobicity and with increasing slip velocity (Fig. 6). Also, to quantify this phenomenon, the curves of streak strength are presented in Fig. 7. As indicated in Fig. 7, the streak strength of the no-slip channel changed from 0° to 45° , while these quantities were nearly 10° to 45° , 15° to 45° , and 17° to 45° for the slips in 30-30, 30-60, and 30-90 micro-featured walls, respectively. From this figure, it is apparent that the near wall streaks of slip cases became stronger than the no-slip viscous sublayer streaks, which was related to increasing near wall velocity due to wall slip velocity. In accordance with Fig. 8(a) and shifting the peak of Q to the bottom wall, it can be concluded that increasing the streak strength of near wall streaks led to decreasing the velocity gradients between the viscous sublayer and the buffer layer streaks and caused the maximum production of quasi-streamwise vortices to move toward the superhydrophobic wall.

The RMSs of the vorticity components are presented in Fig. 8(b)-(d). These figures show that the RMSs of the streamwise and spanwise vorticities were decreased, and the peak of ω_{x-RMS} was shifted to the bottom wall. The alternations of ω_{x-RMS} were in agreement with the Q profile, i.e., the quasi-streamwise vortices were weakened, and the place of the maximum presence of these vortices was moved toward the bottom wall. Also, according to the increasing ejection of the low-speed streak in the viscous sublayer and its decrease in the buffer layer (Fig. 11(a)), the RMS of the wall-normal component of vorticity was increased in the viscous sublayer and decreased in the buffer layer. These changes confirmed that the quasi-streamwise vortices were shifted to the bottom wall and the ejection of low-speed streaks was increased in the viscous sublayer and decreased in the buffer layer (Fig. 11(a)). The non-zero quantities of ω_{y-RMS} at the wall were due to the presence of partial streamwise slip fluctuations at the bottom wall.

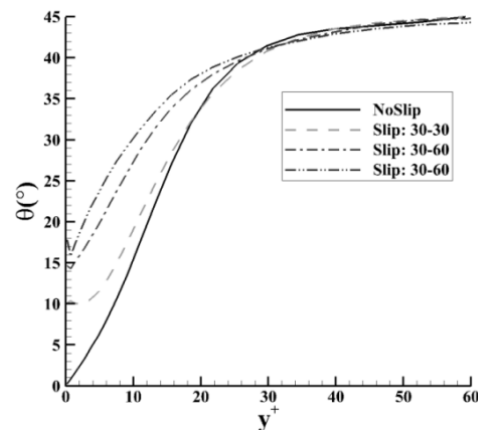


Fig. 7. Streak strength averaged in the x and z directions.

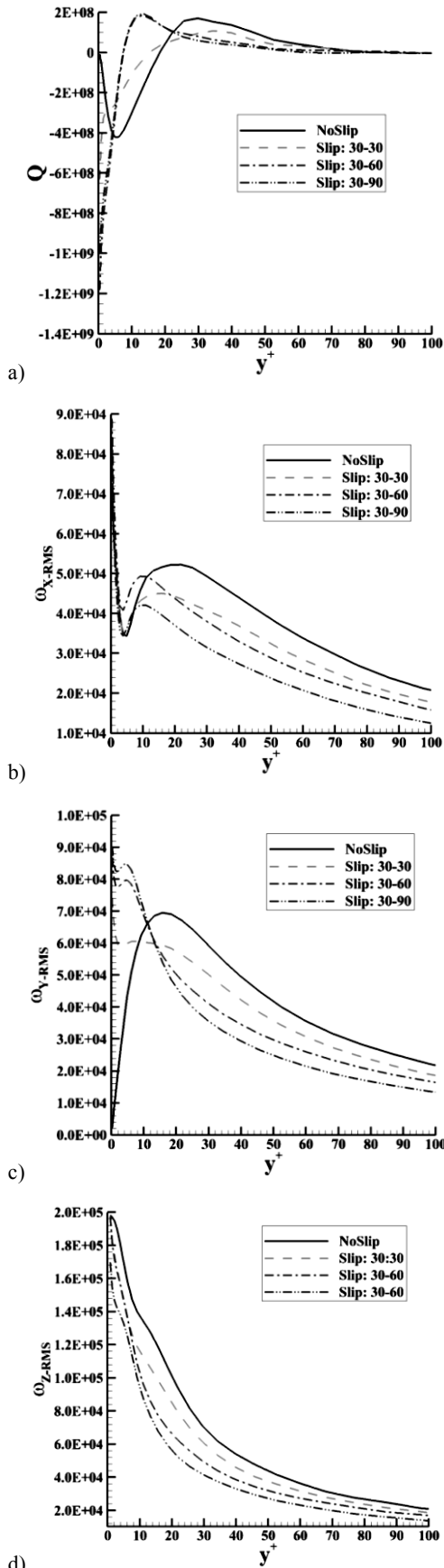


Fig. 8. (a) Mean profile of Q ; RMS profile of (b) ω_x -RMS ; (c) ω_y -RMS ; (d) ω_z -RMS .

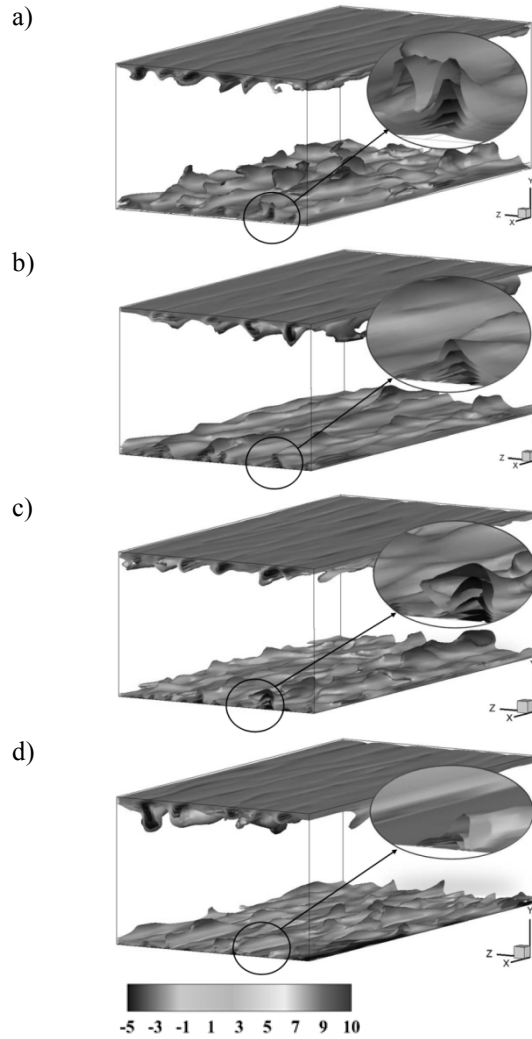


Fig. 9. Lifted low-speed streaks indicated by streamwise velocity isosurfaces colored by streamwise velocity fluctuation: (a) no-slip; (b) slip: 30-30; (c) slip: 30-60; (d) slip: 30-90.

The qualitative representation of the lifted low-speed streaks was indicated by the streamwise velocity isosurfaces, as presented in Fig. 9. It is clear from these isosurfaces that the lifted, low-speed streaks were smoothed and that the upward motion of the low-speed streaks was limited to the lower values of wall distance.

The quadrant analysis of the Reynolds shear stress presented detailed information on the contribution of various events occurring in the flows to the total turbulence production (Türk *et al.* 2014) and Wallace *et al.* (1972)). The analysis divided the Reynolds shear stress into four classifications according to the signs of u' and v' . The first quadrant, $u' > 0$ and $v' > 0$, contains outward motion of high-speed fluid; the second quadrant, $u' < 0$ and $v' > 0$, contains the motion associated with ejections of low-speed fluid away from the wall; the third quadrant, $u' < 0$ and $v' < 0$, includes inward motion of low-speed fluid; and the fourth quadrant, $u' > 0$ and $v' < 0$, has an inrush

of high-speed fluid, sometimes referred to as the sweep event. Thus, the second- and fourth-quadrant events contribute to the negative Reynolds shear stress (positive production), and the first- and third-quadrant events contribute to the positive Reynolds shear stress (negative production) (Kim *et al.* (1987)). The no-slip results displayed the dominance of the ejection event (second quadrant, $u' < 0$ and $v' > 0$) away from the wall with the sweep event (fourth quadrant, $u' > 0$ and $v' < 0$) dominating in the wall region; at $y^+ \approx 19$, they were about the same. The contribution to the Reynolds shear stress from each quadrant as a function of y^+ location is shown in Fig. 11(a) and (b). In this figure the triangular brackets are spatially averaged (the Eq. (3)) and the normalization is done using the time averaged quantities (same as values in are presented in the Fig. 5). The ejection of low-speed fluid increased in the region below $y^+ \approx 20$ and decreased in the buffer layer (Fig. 11(a)). While the sweep event was increased in the slip cases (Fig. 11(b)), the increased ejection was more than sweep. Increasing ejection and sweep in the viscous sublayer confirmed the approach of the quasi-streamwise vortices to the bottom wall. Since the ejection and sweep were the dominant contributors to the Reynolds stress, it was expected that the turbulence production and Reynolds stress to increase with increasing ejection and sweep, while it was in contrast with the decreasing Reynolds stress (Fig. 5(d)) and turbulence production (Fig. 12(a)). This contradiction was revealed in Q1 (Fig. 11(c) and Q3 (Fig. 11(d)). As shown in Fig. 11(c) and (d), the outward motion of high-speed fluid (Q1) and inward motion of low-speed fluid (Q3) were increased as well, while these increases were more than ejection and sweep and could result in the viscous dissipation of turbulent kinetic energy more than no-slip channel (Fig. 12(b)). The production of turbulent kinetic energy and viscous dissipation are presented in Fig. 12. As is clear in this figure, increased Q1 and Q3 were more effective than Q2 and Q3 events and resulted in increased viscous dissipation as well as decreased turbulence production (Fig. 12(a)).

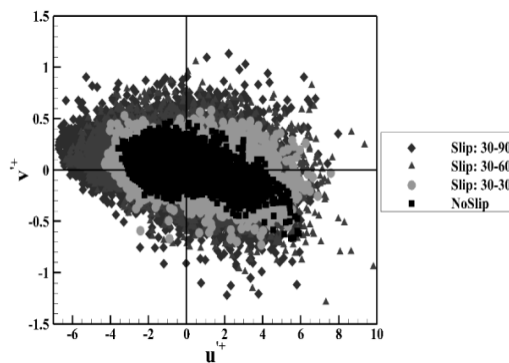


Fig. 10. Quadrant plot for Reynolds shear stress at $y^+ = 5$.

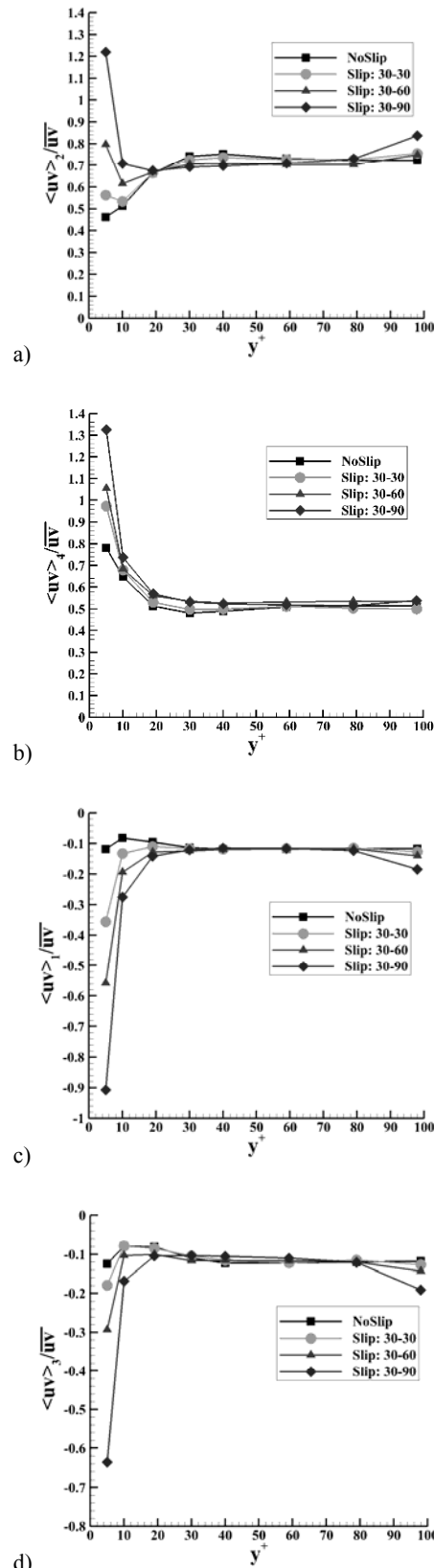


Fig. 11. Reynolds shear stress from each quadrant normalized by the local mean Reynolds shear stress; subscripts 1, 2, 3, and 4 are the first, second, third, and fourth quadrants, respectively.

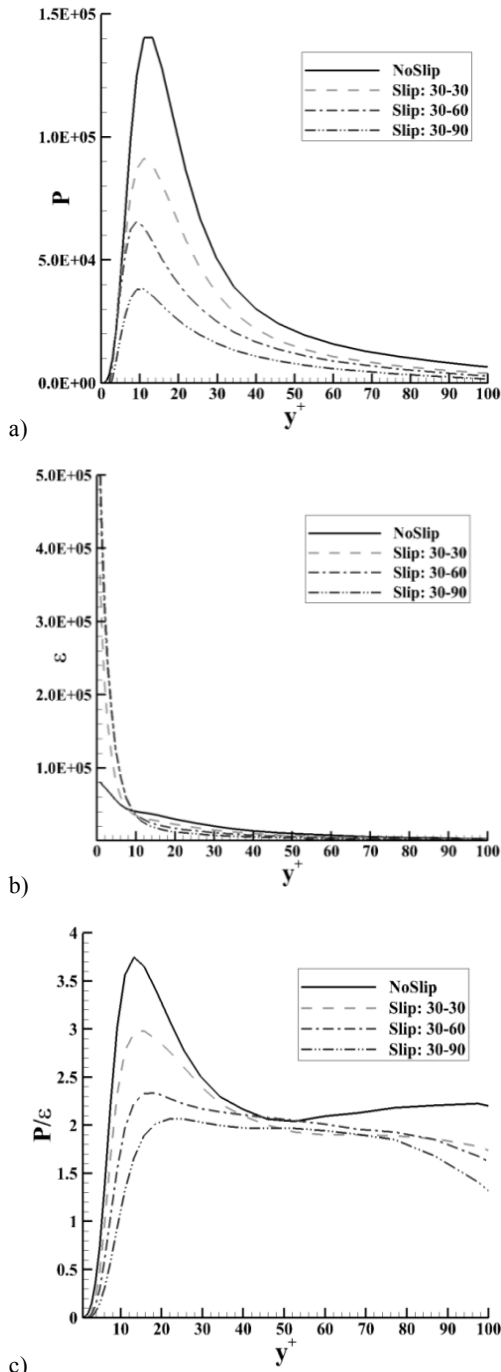


Fig. 12. (a) Production of turbulent kinetic energy (P); (b) viscous dissipation (ε); (c) ratio of production to dissipation of turbulent kinetic energy.

One of the most important parameters of turbulent flow is correlations. Spatial correlation coefficients were investigated to evaluate the modifications of turbulent structures. The spanwise, two-point correlation coefficients are defined as follows:

$$R_{u_i, u_j}(\Delta z) = \frac{\overline{u_i(z)u_j(z + \Delta z)}}{\sqrt{\overline{u_i^2(z)}}\sqrt{\overline{u_j^2(z + \Delta z)}}} \quad (11)$$

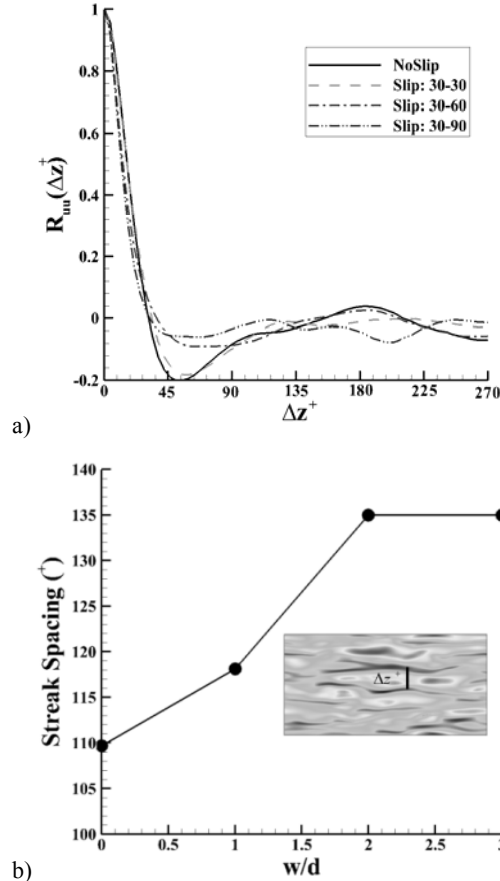


Fig. 13. (a) Lateral two-point correlations for streamwise velocity fluctuation at y⁺ = 10; (b) Streak spacing in the wall units at y⁺ = 10.

Where $i, j = 1, 2$, and 3 , respectively. Fig. 13(a) illustrates the spatial two-point correlation coefficient of the streamwise velocity fluctuation in the spanwise direction at $y^+ = 10$. The no-slip correlation coefficient becomes negative and reaches its minimum at $\Delta z^+ \approx 55$ (Fig. 13(a)). The term Δz^+ , at which this minimum occurs, provides an estimate of the mean separation between high-speed and low-speed flow, and the mean spacing between the streaks is roughly twice the distance (Kim *et al.* 1987). As can be seen in Fig. 13(a), the minimum of $R_{uu}(\Delta z)$ was shifted to the larger values of Δz , implying that the distance between streaks was increased due to superhydrophobicity. Distances of streaks at $y^+ = 10$ were extracted from the minimum of the $R_{uu}(\Delta z)$, and they are presented in Fig. 13(b). 0(a) shows the two-point correlation coefficient of the wall-normal velocity fluctuation in the spanwise direction at $y^+ = 10$. The no-slip correlation coefficient became negative and reached its minimum at $\Delta z^+ \approx 29$ (0(a)). The Δz^+ at which this minimum occurred corresponded to the streamwise vortex diameter

(Kim *et al.* (1987)). As shown in this figure, the vortex diameter for micro-featured surfaces was increased and enlarged with increasing w/d . The spatial two-point correlation coefficient of the spanwise velocity in the spanwise direction $y^+ = 10$ is shown in 0(b). The minimum of these correlation coefficients, which corresponds to counter-rotating vortex pairs (Kim *et al.* (1987)), is shifted to larger values in Δz . This means that the distance between vortex pairs increases due to superhydrophobicity, which is consistent with the streamwise vortical structures, approaching the lower wall values.

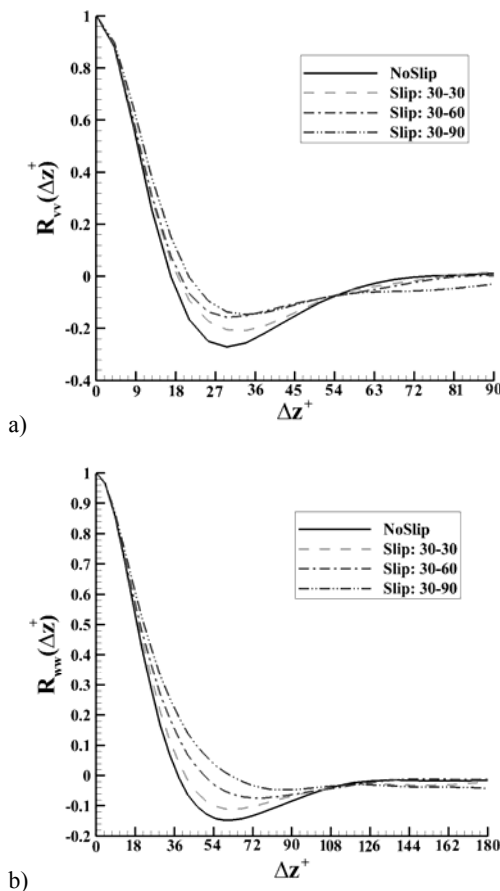


Fig. 14. (a) Lateral two-point correlations for wall-normal velocity fluctuation at $y^+ = 10$; (b) Lateral two-point correlations for the spanwise velocity fluctuation at $y^+ = 10$.

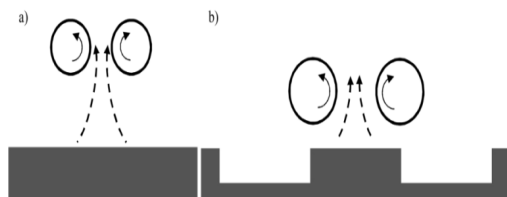


Fig. 15. Schematic of the quasi-streamwise vortex: (a) no-slip wall; (b) micro-featured superhydrophobic surfaces.

5. CONCLUSIONS

The main objective of this study was to reveal the underlying mechanisms of turbulent structure alternations due to the employment of the streamwise micro-featured superhydrophobic wall. The LES of fully-developed turbulent channel flow was considered to explore micro-features' role in the near-wall turbulent statistics. For this purpose, the no-slip condition at the bottom wall of the regular channel was replaced by a shear-free condition, which was only applied to the air-water interface. The influences of the micro-featured surface on the mean velocity profile, drag reduction, and slip velocity also were investigated. The slip velocity was increased with w/d from 23 to 57% of the bulk velocity for $w/d = 1$ to 3. Drag reductions were nearly 10, 18, and 26% for $w/d = 1, 2,$ and 3, respectively. By applying the triple decomposition of the velocity field to the superhydrophobic channels, the following conclusions were achieved:

The turbulent drag reduction decreased the viscous sublayer velocity gradient and affected the streak instability cycle and production of the streamwise vortical structures.

The second order turbulence statistics showed that the peak of Reynolds stresses decreased and got closer to the superhydrophobic wall.

The outward motion of the lifted low-speed streaks was restricted to the lower wall layers, and the region of maximum production of streamwise vortices was shifted to the micro-featured wall.

Comparison of coherent structures showed that the density of near-wall coherent structures was reduced and the location of their maximum existence was shifted to the bottom wall.

The results indicated that increased streak strength did not result in stronger generation of turbulence, while the Reynolds shear stress and streamwise vorticity were weakened. The quadrant analysis of Reynolds stress showed that the stronger increase of the outward motion of high-speed fluid (Q1) and the inward motion of low-speed fluid (Q3), in comparison with ejection (Q2) and sweep (Q4), resulted in more viscous dissipation of turbulent kinetic energy and decreased the turbulence production.

The correlation coefficients indicated that the spanwise distance of lifted low-speed streaks was increased. The near-wall streamwise vortical structures were increased in diameter, and the distance between counter-rotating vortices was increased to some extent.

However, it should be mentioned that these findings are limited to the streamwise orientation of features and cannot be extended to other orientations; thus, further studies should be performed.

REFERENCES

Busse, A. and N. D. Sandham (2012). Influence of an anisotropic slip-length boundary condition

- on turbulent channel flow. *Physics of Fluids*. 24(5), 055111.
- Fukagata, K., N. Kasagi and P. A. Koumoutsakos (2006). theoretical prediction of friction drag reduction in turbulent flow by superhydrophobic surfaces. *Physics of Fluids*. 18(5), 051703.
- Germano, M., U. Piomelli, P. Moin, W. H. A. Cabot (1991). dynamic subgrid-scale eddy viscosity model. *Physics of Fluids A: Fluid Dynamics*. 3(7), 1760-5.
- Jeffs, K., D. Maynes and B. W. Webb (2010). Prediction of turbulent channel flow with superhydrophobic walls consisting of micro-ribs and cavities oriented parallel to the flow direction. *International Journal of Heat and Mass Transfer*. 53(4), 786-96.
- Jeong, J. and F. Hussain (1995). On the identification of a vortex. *Journal of fluid mechanics*. 285, 69-94.
- Jiménez, J. and A. Pinelli (1999). The autonomous cycle of near-wall turbulence. *Journal of Fluid Mechanics*. 389, 335-59.
- Kim, J., P. Moin and R. Moser (1987). Turbulence statistics in fully developed channel flow at low Reynolds number. *Journal of fluid mechanics*. 177, 133-66.
- Lu, S. S., W.W. Willmarth (1973). Measurements of the structure of the Reynolds stress in a turbulent boundary layer. *Journal of Fluid Mechanics*. 60(03), 481-511.
- Martell, M. B., J. B. Perot, J. P. Rothstein (2009). Direct numerical simulations of turbulent flows over superhydrophobic surfaces. *Journal of Fluid Mechanics*. 620, 31-41.
- Martell, M. B., J. P. Rothstein and J. B. Perot (2010). An analysis of superhydrophobic turbulent drag reduction mechanisms using direct numerical simulation. *Physics of Fluids*. 22(6), 065102.
- Min, T. and J. Kim (2004). Effects of hydrophobic surface on skin-friction drag. *Physics of Fluids* 16(7), L55-8.
- Nouri, N. M., M. S. Bakhsh and S. Sekhavat (2013). Analysis of shear rate effects on drag reduction in turbulent channel flow with superhydrophobic wall. *Journal of Hydrodynamics, Ser. B*. 25(6), 944-53.
- Nouri, N. M., S. Sekhavat and A. Mofidi (2012). Drag reduction in a turbulent channel flow with hydrophobic wall. *Journal of Hydrodynamics, Ser. B*. 24(3), 458-66.
- Park, H., H. Park and J. Kim (2013). A numerical study of the effects of superhydrophobic surface on skin-friction drag in turbulent channel flow. *Physics of Fluids*. 25(11), 110815.
- Philip, J. R. (1972). Integral properties of flows satisfying mixed no-slip and no-shear conditions. *Zeitschrift für angewandte Mathematik und Physik ZAMP*. 23(6), 960-8.
- Reynolds, W. C. and A. K. Hussain (1972). The mechanics of an organized wave in turbulent shear flow. Part 3. Theoretical models and comparisons with experiments. *Journal of Fluid Mechanics*. 54(02), 263-88.
- Schoppa, W. and F. Hussain (2002). Coherent structure generation in near-wall turbulence. *Journal of Fluid Mechanics*. 453, 57-108.
- Türk, S., G. Daschiel, A. Stroh, Y. Hasegawa and B. Frohnäpfel (2014). Turbulent flow over superhydrophobic surfaces with streamwise grooves. *Journal of Fluid Mechanics*. 747, 186-217.
- Wallace, J. M., H. Eckelmann and R. S. Brodkey (1972). The wall region in turbulent shear flow. *Journal of Fluid Mechanics*. 54(01), 39-48.
- Ybert, C., C. Barentin, C. Cottin-Bizonne, P. Joseph and L. Bocquet (2007). Achieving large slip with superhydrophobic surfaces: Scaling laws for generic geometries. *Physics of Fluids*. 19(12), 123601.